Received 7 August 2022; accepted 26 August 2022. Date of publication 31 August 2022; date of current version 16 November 2022.

Digital Object Identifier 10.1109/OJCOMS.2022.3203162

Error Analysis of the Joint Localization and Synchronization of RIS-Assisted *mm*-Wave MISO-OFDM Under the Effect of Hardware Impairments

BUSRA CENIKLIOGLU [1] (Graduate Student Member, IEEE), DEEB ASSAD TUBAIL [2], AYSE ELIF CANBILEN [3] (Member, IEEE), IBRAHIM DEVELI [4] (Senior Member, IEEE), AND SALAMA S. IKKI [2] (Senior Member, IEEE)

[1]Department of Electrical and Electronics Engineering, Nuh Naci Yazgan University, 38040 Kayseri, Turkey

[2]Electrical and Computer Engineering Department, Lakehead University, Thunder Bay, ON P7B 7C3, Canada

[3]Department of Electrical and Electronics Engineering, Konya Teknik Universitesi, 42250 Konya, Turkey

[4]Department of Electrical and Electronics Engineering, Erciyes University, 38039 Kayseri, Turkey

CORRESPONDING AUTHOR: B. CENIKLIOGLU (e-mail: bceniklioglu@nny.edu.tr)

This work was supported by the Scientific and Technological Research Council of Turkey (TUBITAK) International Doctoral Research Fellowship Program under Grant BIDEB-2214.

ABSTRACT This work investigates the theoretical bounds of the joint localization and synchronization processes in a reconfigurable intelligent surface (RIS)-assisted system. We address the case of millimeter-wave (*mm*-Wave) multiple-input single-output (MISO) orthogonal frequency-division multiplexing (OFDM) with non-ideal transceivers. Considering a single antenna mobile station (MS) aims to estimate the parameters of the downlinks from the base station (BS) and the RIS by observing a known sequence received by the MS directly from the BS and indirectly through the RIS. The theoretical bounds of the estimation process are assessed by using the Fisher information matrix (FIM). A transformation matrix is then used to convert the FIM of the downlink channel parameters to the FIM of the MS joint localization and synchronization parameters. Specifically, the transformation matrix is derived based on the geometric relationships that convert the estimated downlink channels' parameters to the position coordinates and clock offset. Next, the Cramer-Rao lower bound (CRLB) matrix of the joint localization and synchronization process is obtained by using the pseudo-inverse of the FIM. Thus, the position error bound (PEB), as well as the synchronization error bound (SEB), are calculated. Computer simulation results are provided to illustrate the adverse effects of the hardware impairments (HWIs) on the accuracy of localization and synchronization. These results are given in proportion to the effective signal-to-noise ratio (SNR), the number of pilot transmissions, and the number of the RIS elements.

INDEX TERMS OFDM, *mm*-wave, localization, synchronization, fisher information matrix, hardware impairments, RIS.

I. INTRODUCTION

THE FIFTH generation (5G) of wireless networks offers unprecedented levels of bandwidth and energy efficiency to ensure seamless and reliable communication between users and many different objects [1]. The use of such a large bandwidth in 5G, along with the deployment of an enormous number of antenna arrays at both the base station (BS) and the mobile station (MS), is expected to improve the accuracy of localization from a single BS [2]. It is therefore no surprise that radio localization has risen to prominence with the launch of 5G technologies such as millimeter-wave (*mm*-Wave) wireless communication systems [3].

Accurate wireless localization has been extensively studied in *mm*-Wave technologies, where it has shown tremendous promise [4], [5]. According to [4], *mm*-Wave technology for 5G systems has the ability to provide so robust an indoor localization scheme that centimeter-accuracy can be ensured. The error bounds for uplink and downlink three dimensional (3D) localization in 5G *mm*-Wave systems were discussed in [5], [6] and following that the authors of [5] studied the further reduction of localization error in *mm*-Wave systems. Moreover, the fundamental bounds on the position and orientation estimation accuracy were derived in [2], showing that *mm*-Wave and large multiple-input multiple-output (MIMO) systems enable accurate positioning and device orientation estimation with only one BS, even when the line-of-sight (LOS) link is blocked. In [7], a method was proposed for the estimation of angle-of-arrival (AOA), angle-of-departure (AOD) and channel gains in the downlink transmission. Also the authors in [8] addressed the problem of positioning based on AOD and AOA estimation and investigated the effect of errors in delays and phase shifters.

On the other hand, reconfigurable intelligent surface (RIS) technology has recently emerged as an innovative way to achieve high energy and spectral efficiency for future communication systems. An RIS is a reconfigurable array of passive reflecting elements, each of which can independently alter the phase and/or attenuation of the incident signal. This ability enables many soft-controlled electromagnetic functionalities (e.g., anomalous reflection and focusing), and makes controllable smart radio environments possible [9]. Also, the RIS systems can provide a good trade-off between the hardware and signal processing complexity. In addition, [10], [11] verified that the RIS is able to enhance the link quality of the conventional setup without the RIS.

Considering that an RIS can also provide great benefits to performance, energy consumption, and cost for mapping and localization, RIS-assisted 5G *mm*-Wave systems were investigated in terms of localization [6], [12], [13], [14], [15]. The position error bound (PEB) and the orientation error bound (OEB) were derived in [12] for a two dimension (2D) RIS-assisted *mm*-Wave localization process, while the PEB was calculated in [6] for a 3D uplink localization process in 5G *mm*-Wave systems, considering of course both synchronous and asynchronous cases. The PEB and OEB were also evaluated in [8], where it was shown that an RIS can significantly enhance the localization performance. The theoretical performance bounds were defined by calculating the Cramer-Rao lower bound (CRLB) for positioning in [13], [16]. The impact of the number of RIS elements was investigated and the value of phase shifters on the position estimation accuracy was compared to the conventional scheme with one LOS and one non-LOS (NLOS) link in [13].

Besides, the RIS deployment both enables and enhances the localization process in different environments. For example, the work in [17] proposed the deployment of multiple aerial intelligent reflecting surfaces (AIRSs) to locate users in a designated outdoor area with no LOS links. This way, LOS links are created between the MS and the AIRSs that measure multiple AoA values to localize the users. Furthermore, RISs are proposed in [18] to create a favorably received signal strength (RSS) distribution in an indoor environment, where based on this favorable RSS distribution, multiple users in that area can localize themselves. More importantly, also it was seen in [14], [19], [20], [21] that the utilization of RIS enables the joint localization and synchronization just by exploiting downlink multiple-input single output (MISO) transmission.

All the above-aforementioned works investigated localization and synchronization estimation under the assumption of ideal hardware. Needless to say that the assumption of ideal transceivers makes vision blurry around the real accuracy of the localization and estimation process since of course, the HWIs always jeopardize performance [22], [23]. The deployment and operation of different types of circuitry operating at high frequencies, e.g., mm-Wave communications, can be severely limited by non-ideal hardware behavior [24], [25].

However, recently, the provided work in [25] presented the CRLB to investigate the hardware impairments (HWIs) impact on the localization process, where this work considered the localization processes through the uplink parameters of the MIMO channel. Similarly, the CRLB of the localization is presented in a MIMO *mm*Wave system under hardware impaired transceivers case in [26]. Besides, both works considered the synchronization process in a prior stage before the localization, however, the early work assumed a perfect synchronization process, while the later work supposed an imperfect synchronization process.

It is well-known that the synchronization process is meant to eliminate the offset between the MS and BS clocks, which is critical for localization accuracy. The localization process is strongly dependent on synchronization because it is performed by measuring the time of flight for the pilot sequence from the BS towards the MS. Therefore, an asynchronous clock would shift this measured value away from the actual one, which would in turn deteriorate the localization accuracy. In the same context, it is worth noting that this synchronization process can be performed either simultaneously with the localization procedure, or as a preliminary step before it.

Furthermore, the presented works in [27], [28], [29] declared that the joint localization-synchronization strategy provides a significant improvement over the traditional sequential approach since there is a close relationship between the two processes, and they can be performed simultaneously with a considerably better accuracy. Besides, joint localization-synchronization can be performed by exchanging only one data package rather than two. This is especially applicable to nodes that have limited power and memory.

In addition, the provided works in [30], [31], [32] proved that the RIS-aided system boosts the performance of both localization and synchronization. Additionally, next-generation cellular networks will witness the creation of smart radio environments (SREs), where walls and objects

can be coated with RISs to strengthen the communication and localization coverage by controlling the reflected multipath. Compared to a conventional system without RIS, it can achieve up to a two-order and one-order magnitude reduction in PEB and SEB values, respectively. The achieved results open the door towards the adoption of the RISs as an effective method for supporting mobile wireless localization and thus, improving communication performance. In particular, the work in [32] demonstrated that the proposed approach can achieve high localization and synchronization accuracy (even in the low SNR region) by adjusting the system parameters, without optimizing neither the transmit beamforming nor the RIS control matrix, and requiring no previous knowledge of the clock offset.

In this context, the achievement of the joint localization-synchronization processes with minimum data exchange and transmission is essential for future 5G networks that crave saving energy and uplink resources. In specific, 5G networkss envision serving a massive number of terminals that need to transmit data to the BS under the Internet of Things (IoT) paradigm, which is expected to overload the uplink (medium access) channel. In response, processing joint localization and synchronization exclusively on-board at the MS instead of at the BS side is proposed. Doing so allows multiple MS to be localized by exploiting the single transmission of a known pilot from the BS (e.g., a broadcast control channel) with no overhead for the system. Furthermore, positioning on MSs boards distributes the localization task and relieves the burden to take over the BS [33].

Seeking an efficient channel estimation in the *mm*Wave systems, the multi-antenna user, and thus the MIMO *mm*Wave scenario, is recommended. This system can compensate for severe path loss by employing high directional beamforming. Unfortunately, recent research showed that it is more likely for massive arrays to be implemented only at the BS side. In that case, the one-antenna MS (and thus the MISO *mm*Wave system), would become more practical [33], [34], [35].

In this case, the time of flight and the angle of departure (AoD) are estimated by the MS from the downlink channel, and this happens instead of performing the time of flight and the angle of arrival (AoA) estimation at the BS side using the uplink channel. Next, these estimated parameters are translated to the joint localization-synchronization process utilizing the known geometric relationships.

The underlying idea behind estimating the AOD on-board the single antenna MS is based on the fact that the different transmitted beams are received with different magnitudes and phases depending on the direction in which the receiver is seen from the transmitter. It is not possible to estimate the AOD using on a single transmitted beam, because the received signal amplitude depends on not only the beam pattern but also the unknown channel amplitude. Where there are multiple transmitted beams, the ratio between the received amplitudes from different beams depend on the beam patterns, not the channel gain. Accordingly, it becomes possible to determine the direction from which the MS is reached, and thus it is possible to estimate the AoD. It is worth mentioning that the multiple beams can be transmitted sequentially (by time division), or at different sub-carriers (by frequency division) [33].

Furthermore, it is well-known that *mm*Wave links are more susceptible to blockages, even those caused by the human body itself, than to lower frequencies. The *mm*Wave research community felt that multi-connectivity could be a solution to overcome such issues in that it allows an MS to maintain multiple possible LOS paths to different BSs. In that case, drops in one link can be overcome by switching data paths. Accordingly, assuming that the MS operates in environments with at least one LOS path to a (non-obstructed) BS is prevalent in the literature, e.g., in [26], [33], [34], [35], [36].

Contributions: Considering the above-mentioned issues, the contributions of this study can be summarized as follows:

- This work presents the CRLB of the joint localization-synchronization process, where the single antenna MS performs the joint localization-synchronization by estimating the downlink channel parameters, i.e., the angles of departure from the BS and RIS, time of flight from the BS to the MS directly, and the time of flight from the BS to the MS through the RIS. It is worth noting that the CRLB presents the most accurate estimation that can be achieved for these parameters, and thus, for the joint localization-synchronization process. Utilizing the estimated downlink parameters and the geometric relationships that will be described later in this work, the MS not only concludes its location but also synchronizes itself to the BS.
- The hardware impairment model representing the imperfectness at the transceivers is introduced, and then, it is integrated into the system model of the RIS-assisted *mm*-Wave MISO-OFDM to present the distorted known pilot that is transmitted from the BS and received by the MS.
- Using the observations collected on distorted pilot, the Fisher Information matrix (FIM) of the estimated parameters is derived, and a transformation matrix is built to transform the FIM of the estimated downlink parameters to the FIM of the position of the MS and clock offset parameters.
- The CRLB of the joint localization-synchronization process is obtained and used to calculate the position error bound (PEB) and synchronization error bound (SEB) terms.

Organization: This paper is organized as follows. Section II incorporates the HWI into the system model. Next, Section III discusses the joint localization and synchronization processes by deriving the FIM and CRLB. Section IV presents and discusses the simulation results, and our final remarks are given in Section V.

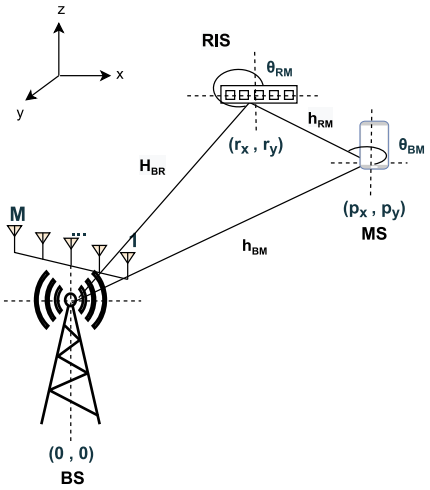

FIGURE 1. RIS-assisted *mm*-wave MISO-OFDM system.

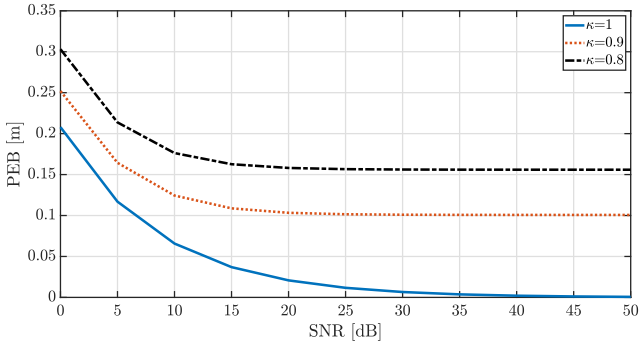

FIGURE 2. PEB v.s the transmission power with different κ in the perfect synchronous system without an RIS.

Notations: Scalars are denoted by lower-case letters, while bold-face lower-case letters are reserved for vectors. Boldface upper-case letters indicate matrices. The element in the ith row and jth column of matrix $\mathbf{A}$ is specified by $[\mathbf{A}]_{(i,j)}$, while the Hermitian and the transpose operators are represented by $(\cdot)^H$ and $(\cdot)^T$, respectively. Besides, $\mathbb{E}\{\cdot\}$ is used for statistical expectations, and $\mathcal{CN}(\mu, \sigma^2)$ represents a complex Gaussian random variable with mean μ and variance σ^2.

II. CHANNEL AND SYSTEM MODELS

Consider a single antenna MS aims at estimating its unknown position $\boldsymbol{p} = [p_x \ p_y]^{\mathrm{T}}$ in RIS-assisted *mm*-Wave MISO-OFDM wireless communication systems. Moreover, consider a known sequence is broadcasted from a known position BS located at $\boldsymbol{q} = [q_x \ q_y]^{\mathrm{T}}$ and that is equipped with M_{B} uniform linear array (ULA) antennas. Similarly, a known position RIS is located at $\boldsymbol{r} = [r_x \ r_y]^{\mathrm{T}}$ and is equipped with M_{R} ULA elements. The complete system is illustrated in Fig. 1, wherein the MS performs the synchronization process is performed jointly with the localization with the help of the known position RIS. Specifically, the RIS creates an NLOS link between the MS and BS, and then the MS localizes and synchronizes its-self by estimating the parameters of both the LOS and NLOS links. Unfortunately, the accuracy of the localization and synchronization processes are affected inversely by the imperfect transceivers of both the BS and MS. Accordingly, the details of the channel model, the HWI model, and the inclusion of the HWI in the system mathematically are presented in this section, respectively.

A. CHANNEL MODEL

The LOS link that exists between the BS and the MS, which provides the highest useful information for positioning is presented in Fig. 1. It is known that this link can be easily isolated based on the received power due to path orthogonality. The complex channel vector associated with the n^{th} sub-carrier, $\mathbf{h}_{\mathrm{BM}}[n] \in \mathbb{C}^{M_{\mathrm{B}} \times 1}$, can be defined as

$$\mathbf{h}_{\mathrm{BM}}[n] = \gamma_{\mathrm{BM}} \boldsymbol{\alpha}(\theta_{\mathrm{BM}}) \exp\Big(-j2\pi n \tfrac{\tau_{\mathrm{BM}}}{NT}\Big), \tag{1}$$

where $n \in \{1, 2, \ldots, N\}$ and N is the total number of sub-carriers, while τ_{BM} is the propagation delay between the BS and MS including clock offset Δ between the BS and the MS. Besides, $T = 1/B$ is the sampling period with B denoting the bandwidth, and $\gamma_{\mathrm{BM}} = \rho_{\mathrm{BM}} e^{j\phi_{\mathrm{BM}}}$ with ρ_{BM} and ϕ_{BM} are being the modulus and the phase of the complex amplitude γ_{BM}. It is worth noting here that the bandwidth B achieves the typical narrow-band condition, i.e., $\lambda_n = c/(\frac{n}{NT} + f_c) \approx \lambda_c = c/f_c$ for $\forall n \in \{1, 2, \ldots, N\}$, where λ_c denotes the wavelength, c and f_c are being the speed of light and the carrier frequency, respectively. Following that the BS array steering vector, $\boldsymbol{\alpha}(\theta_{\mathrm{BM}})$ is a function of the AOD, θ_{BM}, and is expressed as

$$\boldsymbol{\alpha}(\theta_{\mathrm{BM}}) = \left[1 e^{j\frac{2\pi}{\lambda_c} d \sin\theta_{\mathrm{BM}}} \cdots e^{j(M_{\mathrm{B}}-1)\frac{2\pi}{\lambda_c} d \sin\theta_{\mathrm{BM}}}\right]^{\mathrm{T}}, \tag{2}$$

where $d = \lambda_c/2$ defines the ULA inter-element spacing.

On the other hand, the existence of the RIS provides an NLOS link between the BS and MS, in which the transmitted signal reaches to the RIS over $\mathbf{H}_{\mathrm{BR}}[n] \in \mathbb{C}^{M_{\mathrm{B}} \times M_{\mathrm{R}}}$ link, and then reflected to the MS through $\mathbf{h}_{\mathrm{RM}}[n] \in \mathbb{C}^{M_{\mathrm{R}} \times 1}$ channel as shown in Fig. 2. Here, the channel between the BS and RIS over the n^{th} sub-carrier can be given by

$$\mathbf{H}_{\mathrm{BR}}[n] = \gamma_{\mathrm{BR}} \boldsymbol{\alpha}(\theta_{\mathrm{BR}}) \big(\boldsymbol{\alpha}(\theta_{\mathrm{RB}})\big)^{\mathrm{T}} \exp\Big(-j2\pi n \tfrac{\tau_{\mathrm{BR}}}{NT}\Big), \tag{3}$$

where $\gamma_{\mathrm{BR}} = \rho_{\mathrm{BR}} e^{j\phi_{\mathrm{BR}}}$ is the complex amplitude of the channel between the BS and RIS, and τ_{BR} is the delay between them. Additionally, considering the AOA, θ_{BR}, and the AOD, θ_{RB}, $\boldsymbol{\alpha}(\theta_{\mathrm{BR}})$ and $\boldsymbol{\alpha}(\theta_{\mathrm{RB}})$ in (3) can be written as

$$\boldsymbol{\alpha}(\theta_{\mathrm{BR}}) = \left[1 e^{j\frac{2\pi}{\lambda_c} d \sin\theta_{\mathrm{BR}}} \cdots e^{j(M_{\mathrm{B}}-1)\frac{2\pi}{\lambda_c} d \sin\theta_{\mathrm{BR}}}\right]^{\mathrm{T}}, \tag{4}$$

$$\boldsymbol{\alpha}(\theta_{\mathrm{RB}}) = \left[1 e^{j\frac{2\pi}{\lambda_c} d \sin\theta_{\mathrm{RB}}} \cdots e^{j(M_{\mathrm{R}}-1)\frac{2\pi}{\lambda_c} d \sin\theta_{\mathrm{RB}}}\right]^{\mathrm{T}}. \tag{5}$$

Following that, the channel between the RIS and MS for the n^{th} sub-carrier is given as

$$\mathbf{h}_{\text{RM}}[n] = \gamma_{\text{RM}}\boldsymbol{\alpha}(\theta_{\text{RM}})\exp\Big(-j2\pi n\tfrac{\tau_{\text{RM}}}{NT}\Big), \tag{6}$$

where τ_{RM} is the delay between the RIS and MS, $\gamma_{\text{RM}} = \rho_{\text{RM}}e^{j\phi_{\text{RM}}}$ is the complex gain over the RIS-MS link, and the array steering vector is given by

$$\boldsymbol{\alpha}(\theta_{\text{RM}}) = \left[1 e^{j\frac{2\pi}{\lambda_c}d\sin\theta_{\text{RM}}} \cdots e^{j(M_{\text{R}}-1)\frac{2\pi}{\lambda_c}d\sin\theta_{\text{RM}}}\right]^{\text{T}}. \tag{7}$$

Consequently, the NLOS link between the BS and MS, $\mathbf{h}^g_{\text{NLOS}}[n] \in \mathbb{C}^{M_{\text{B}}\times 1}$, is given by

$$\mathbf{h}^g_{\text{NLOS}}[n] = \mathbf{H}_{\text{BR}}[n]\Omega^g\mathbf{h}_{\text{RM}}[n], \tag{8}$$

where Ω^g is the phase control matrix of the RIS at transmission g, which is a diagonal matrix with unit-modulus entries, i.e., $\Omega^g = \text{diag}([e^{j\omega^g_1}, \ldots, e^{j\omega^g_{M_{\text{R}}}}])$, for $\Omega^g \in \mathbb{C}^{M_{\text{R}}\times M_{\text{R}}}$.

Moreover, the entire channel that includes both the LOS and NLOS links between the BS and MS for the nth sub-carrier at gth transmission, can be written by

$$\mathbf{h}^g[n] = \mathbf{h}_{\text{BM}}[n] + \mathbf{H}_{\text{BR}}[n]\Omega^g\mathbf{h}_{\text{RM}}[n]. \tag{9}$$

B. HARDWARE IMPAIRMENT MODEL

Despite many calibration and/or pre-processing steps that are practically performed to compensate and absorb the HWIs, an unavoidable amount of distortion, referred to as *residual* HWI, typically remains for all practical scenarios, and can still cause significant performance degradation [22]. In order to investigate the impact of the residual HWIs on the system performance, the behavior of the HWIs is modeled in many works as a non-linear memoryless function.

The non-linear memoryless model is presented in [22], where the output of this model is given by

$$y = \sqrt{P\kappa}x + \eta. \tag{10}$$

In the worst-case scenario, the distortion term, $\eta \sim \mathcal{CN}(0, P(1-\kappa))$, is independent of the input x. Then, the distortion power is proportional to the input power P with proportionality constant $(1-\kappa)$.[1] Thus, $\mathbb{E}\{|y|^2\} = \kappa\text{P}+(1-\kappa)\text{P} = \text{P}$ for any value of the hardware quality factor $\kappa \in (0, 1]$. It is worth noting that the HWI coefficients are calculated from the error vector magnitude (EVM), which is specified in the data sheets of the RF components [22]. Moreover, $\kappa = 1$ represents the case of ideal hardware, which results in $y = \sqrt{P}x$.

1. This occurs because the compensation algorithms typically used to mitigate hardware impairments are calibrated to make the average power of the input and output equal [22].

C. SYSTEM MODEL IN THE PRESENCE OF HWI

To investigate how the quality of hardware components affects the accuracy of the joint localization and synchronization processes in the RIS-assisted *mm*-wave MISO-OFDM system, the HWI model is incorporated into the transmitter of the BS as well as into the receiver of the MS. Considering the residual HWI effects, the transmitter and the receiver are modeled in this section, respectively.

1) THE TRANSMITTER MODEL

The joint localization and synchronization processes are performed based on a well-known signal that is conveyed from the BS through K OFDM symbols over N different sub-carriers with G sequential transmissions. During the g^{th} transmission over the n^{th} sub-carrier, the OFDM symbols, $z^g[n] = [z^g_1[n], \ldots, z^g_K[n]]^{\text{T}}$, are transmitted with power P. These symbols are transformed to the time-domain and then combined with a cyclic prefix (CP) before precoding using the hybrid beamforming matrix $\mathbf{F}^g[n]$. The transmitter hybrid beamforming matrix $\mathbf{F}^g[n] \in \mathbb{C}^{M\times k} = \mathbf{F}_{\text{RF}}\mathbf{F}^g_{\text{BB}}[n]$ has a power constraint of $\|\mathbf{F}^g[n]\|_{\text{F}} = 1$, and is applied using a hybrid architecture to lower the hardware complexity. Assuming that L chains are available at the BS, $\mathbf{F}^g_{\text{BB}}[n] \in \mathbb{C}^{L\times M}$ is the digital beamformer, while $\mathbf{F}_{\text{RF}} \in \mathbb{C}^{M\times L}$ is implemented using analog phase shifters. Here, $[\mathbf{F}_{\text{RF}}]_{(m,l)} = e^{j\phi_{(m,l)}}$, while $\phi_{(m,l)}$ is being a given phase for $m = 1, \ldots, M$ and $l = 1, \ldots, L$ [33], [37].

Considering that the BS suffers from HWI with a hardware quality factor coefficient κ_t, the transmitted signal from the BS at the gth transmission over the nth sub-carrier can be expressed as

$$\mathbf{s}^g[n] = \sqrt{\kappa_t}\mathbf{F}^g[n]z^g[n] + \boldsymbol{\eta}^g_t[n], \tag{11}$$

where $\boldsymbol{\eta}^g_t[n] \in \mathbb{C}^{M_{\text{B}}\times 1}$ is the distortion term, which follows a zero-mean complex Gaussian distribution with $\mathbb{E}\{\|\boldsymbol{\eta}^g_t[n]\|^2\} = P(1-\kappa_t)\ \forall n$, and $\mathbb{E}\{\|\mathbf{s}^g[n]\|^2\} = P\ \forall n$.

2) THE RECEIVER MODEL

When the transmitted signal reaches to the MS, firstly the CP is removed and the fast Fourier transform (FFT) is applied. Then, considering (1) and (11), the conveyed signal from the BS to the MS over the LOS link can be written as follows

$$r^g_{\text{LOS}}[n] = \sqrt{\kappa_t}\big(\boldsymbol{h}_{\text{BM}}[n]\big)^{\text{T}}\boldsymbol{F}^g[n]z^g[n] + \big(\boldsymbol{h}_{\text{BM}}[n]\big)^{\text{T}}\boldsymbol{\eta}^g_t[n] \tag{12}$$

while based on (8) and (11), the received signal over the NLOS link is given by

$$\begin{aligned} r^g_{\text{NLOS}}[n] = {} & \sqrt{\kappa_t}\big(\mathbf{h}_{\text{RM}}[n]\big)^{\text{T}}\Omega^g\big(\mathbf{H}_{\text{BR}}[n]\big)^{\text{T}}\mathbf{F}^g[n]z^g[n] \\ & + \big(\mathbf{h}_{\text{RM}}[n]\big)^{\text{T}}\Omega^g\big(\mathbf{H}_{\text{BR}}[n]\big)^{\text{T}}\boldsymbol{\eta}^g_t[n]. \end{aligned} \tag{13}$$

According to the HWI model given in (10), the total received signal at the MS, $r^g_{\text{LOS}}[n] + r^g_{\text{NLOS}}[n]$, is multiplied by the receiver hardware quality factor $\kappa_r \in (0, 1]$, and independent distortion noise is added to that. Therefore, the

received signal at the MS in the presence of the HWIs is written as follows

$$\begin{aligned} y^g[n] &= \sqrt{\kappa_t}\sqrt{\kappa_r}\big(\mathbf{h}_{\mathrm{BM}}[n]\big)^{\mathrm{T}}\mathbf{F}^g[n]\mathbf{z}^g[n] \\ &+ \sqrt{\kappa_t}\sqrt{\kappa_r}\big(\mathbf{h}_{\mathrm{RM}}[n]\big)^{\mathrm{T}}\Omega^g\big(\mathbf{H}_{\mathrm{BR}}[n]\big)^{\mathrm{T}}\mathbf{F}^g[n]\mathbf{z}^g[n] \\ &+ \sqrt{\kappa_r}\big(\mathbf{h}_{\mathrm{RM}}[n]\big)^{\mathrm{T}}\Omega^g\big(\mathbf{H}_{\mathrm{BR}}[n]\big)^{\mathrm{T}}\boldsymbol{\eta}_t^g[n] \\ &+ \sqrt{\kappa_r}\big(\mathbf{h}_{\mathrm{BM}}[n]\big)^{\mathrm{T}}\boldsymbol{\eta}_t^g[n] + \eta_r^g[n] + w^g[n], \end{aligned} \tag{14}$$

where $w^g[n] \sim \mathcal{CN}(0, \sigma^2)$ denotes the additive white Gaussian noise (AWGN), while $\eta_r^g[n] \sim \mathcal{CN}(0, C_{\eta_r})$ represents the receiver HWI distortion. Here, C_{η_r} indicates the noise power arising from the HWIs at the receiver side and it can be expressed by

$$C_{\eta_r} = P_{\mathrm{r}}(1-\kappa_r), \tag{15}$$

where P_{r} is the total received power at the MS, which can be given as follows

$$P_{\mathrm{r}} = P_{\mathrm{LOS}} + P_{\mathrm{NLOS}} = PM_{\mathrm{B}}\Big(\rho_{\mathrm{BM}}^2 + M_{\mathrm{R}}^2\rho_{\mathrm{BR}}^2\rho_{\mathrm{RM}}^2\Big). \tag{16}$$

Here, P_{LOS} denotes the received power of the signal passing through the LOS link as shown in (12), and it is written as

$$P_{\mathrm{LOS}} = PM_{\mathrm{B}}\rho_{\mathrm{BM}}^2. \tag{17}$$

In addition to that, P_{NLOS} in (16) is the received power of the signal coming to the MS over the NLOS link as shown in (13), and it is equal to

$$P_{\mathrm{NLOS}} = PM_{\mathrm{B}}M_{\mathrm{R}}^2\rho_{\mathrm{BR}}^2\rho_{\mathrm{RM}}^2. \tag{18}$$

Moreover, based on (14), the noise power at the receiver stemming from the transmitter HWIs can be calculated from

$$C_{\eta_t} = P\kappa_r(1-\kappa_t)M_{\mathrm{B}}\Big(\rho_{\mathrm{BM}}^2 + M_{\mathrm{R}}^2\rho_{\mathrm{BR}}^2\rho_{\mathrm{RM}}^2\Big), \tag{19}$$

and thus, the total noise power of the received signal given in (14) is obtained as follows

$$\begin{aligned} C_y &= C_{\eta_t} + C_{\eta_r} + \sigma^2 \\ &= P(1-\kappa_t\kappa_r)M_{\mathrm{B}}\Big(\rho_{\mathrm{BM}}^2 + M_{\mathrm{R}}^2\rho_{\mathrm{BR}}^2\rho_{\mathrm{RM}}^2\Big) + \sigma^2. \end{aligned} \tag{20}$$

Consequently, $y^g[n] \sim \mathcal{CN}(\varphi^g[n], C_y)$, the mean of which is equal to the noiseless signal that can be defined as

$$\begin{aligned} \varphi^g[n] &= \sqrt{\kappa_t}\sqrt{\kappa_r} \\ &\times \Big[\big(\mathbf{h}_{\mathrm{BM}}[n]\big)^{\mathrm{T}} + \big(\mathbf{h}_{\mathrm{RM}}[n]\big)^{\mathrm{T}}\Omega^g\big(\mathbf{H}_{\mathrm{BR}}[n]\big)^{\mathrm{T}}\Big]\mathbf{F}^g[n]\mathbf{z}^g[n]. \end{aligned} \tag{21}$$

Now, the SNR value at the MS can be written as follows

$$\mathrm{SNR} = \frac{\kappa_t\kappa_r M_{\mathrm{B}}\Big(\rho_{\mathrm{BM}}^2 + M_{\mathrm{R}}^2\rho_{\mathrm{BR}}^2\rho_{\mathrm{RM}}^2\Big)}{(1-\kappa_t\kappa_r)M_{\mathrm{B}}\Big(\rho_{\mathrm{BM}}^2 + M_{\mathrm{R}}^2\rho_{\mathrm{BR}}^2\rho_{\mathrm{RM}}^2\Big) + \big(\sigma^2/P\big)}. \tag{22}$$

Here, as the power of the OFDM symbols increases, i.e., $P \to \infty$, an asymptotic value of the SNR can be calculated from

$$\lim_{P\to\infty}\mathrm{SNR} = \frac{\kappa_t\kappa_r M_{\mathrm{B}}\Big(\rho_{\mathrm{BM}}^2 + M_{\mathrm{R}}^2\rho_{\mathrm{BR}}^2\rho_{\mathrm{RM}}^2\Big)}{(1-\kappa_t\kappa_r)M_{\mathrm{B}}\Big(\rho_{\mathrm{BM}}^2 + M_{\mathrm{R}}^2\rho_{\mathrm{BR}}^2\rho_{\mathrm{RM}}^2\Big)}. \tag{23}$$

It is worth mentioning here that (23) results in $\lim_{P\to\infty}\mathrm{SNR} \to \infty$ in the case of ideal hardware, i.e., $\kappa_t = \kappa_r = 1$.

III. CRAMER-RAO LOWER BOUND (CRLB) ANALYSIS

This section analyzes the performance of the joint localization and synchronization processes of the RIS-assisted *mm*-wave MISO OFDM systems in terms of the CRLB that provides a lower bound for the estimation of the variance of an unbiased estimator. Therefore, initially, this section presents the estimated parameters that are required for the joint localization and synchronization process. Then it derives the Fisher information matrix (FIM) that measures the amount of information about the estimated parameter by observing $y^g[n]$ in (14). After that, the FIM of the estimated parameters are transformed to the FIM of the joint localization and estimation processes. Next, the CRLB matrix of the joint localization and synchronization process is obtained by using the pseudoinverse of the FIM [38]. Finally, the position error bound and the synchronization error bound terms are calculated from the joint localization and synchronization CRLB matrix. It is worthy of note that here, the CRLB bounds are derived considering the HWI of the transceivers at both the MS and BS.

To perform the joint localization and synchronization process, the MS estimates the TOAs (τ_{BM} and τ_{RM}) and AODs (θ_{BM} and θ_{RM}) of the BS. Consequently, the unknown channel parameters vector of the RIS-assisted *mm*-wave MISO-OFDM scheme is as follows

$$\boldsymbol{\beta} = \big[\tau_{\mathrm{BM}}\ \ \theta_{\mathrm{BM}}\ \ \rho_{\mathrm{BM}}\ \ \phi_{\mathrm{BM}}\ \ \tau_{\mathrm{RM}}\ \ \theta_{\mathrm{RM}}\ \ \rho_{\mathrm{R}}\ \ \phi_{\mathrm{R}}\big]^{\mathrm{T}}, \tag{24}$$

while the vector of the joint localization and synchronization parameters is given by

$$\boldsymbol{\mu} = \big[p_x\ \ p_y\ \ \rho_{\mathrm{BM}}\ \ \phi_{\mathrm{BM}}\ \ \rho_{\mathrm{R}}\ \ \phi_{\mathrm{R}}\ \ \Delta\big]^{\mathrm{T}}. \tag{25}$$

Then, the MS jointly localizes and synchronizes its-self through the geometric relationships that are given as follows

$$\begin{aligned} \tau_{\mathrm{BM}} &= \frac{\sqrt{p_x^2 + p_y^2}}{c} + \Delta, \\ \theta_{\mathrm{BM}} &= \mathrm{atan2}\big(p_y, p_x\big), \\ \theta_{\mathrm{BR}} &= \mathrm{atan2}\big(r_y, r_x\big), \\ \theta_{\mathrm{RB}} &= -\pi + \theta_{\mathrm{BR}}, \\ \theta_{\mathrm{RM}} &= \mathrm{atan2}\Big(\big(p_y - r_y\big), \big(p_x - r_x\big)\Big), \\ \tau_{\mathrm{BR}} + \tau_{\mathrm{RM}} &= \frac{\sqrt{r_x^2 + r_y^2}}{c} + \frac{\sqrt{\big(p_x - r_x\big)^2 + \big(p_y - r_y\big)^2}}{c} + \Delta. \end{aligned} \tag{26}$$

where $\rho_{\mathrm{R}} = \rho_{\mathrm{BR}}\rho_{\mathrm{RM}}$ and $\phi_{\mathrm{R}} = \phi_{\mathrm{BR}} + \phi_{\mathrm{RM}}$.

Now, the elements of the symmetric FIM of the unknown channel parameters vector $\mathbf{J}_\beta \in \mathbb{R}^{8\times 8}$, are calculated from

$$[\mathbf{J}_\beta]_{(i,j)} = \sum_{g=1}^{G}\sum_{n=0}^{N-1} \Re\left\{ \left(\frac{\partial \varphi^g[n]}{\partial \beta_i}\right)^{\mathrm{H}} C_y^{-1} \left(\frac{\partial \varphi^g[n]}{\partial \beta_j}\right)\right\} + \frac{1}{2}\mathrm{tr}\left[C_y^{-1}\frac{\partial C_y}{\partial \beta_i} C_y^{-1}\frac{\partial C_y}{\partial \beta_j}\right], \tag{27}$$

where the noiseless signal $\varphi^g[n]$ is given in (21), while the noise variance C_y is defined in (20). Thus, the derivatives of the noiseless signal $\varphi^g[n]$ with respect to the channel parameters vector β are obtained as

$$\begin{aligned}
\frac{\partial \varphi^g[n]}{\partial \tau_{\mathrm{BM}}} &= \frac{-j2\pi n}{NT}\rho_{\mathrm{BM}} e^{j\phi_{\mathrm{BM}}} e^{-j2\pi n\frac{\tau_{\mathrm{BM}}}{NT}} \alpha(\theta_{\mathrm{BM}})^{\mathrm{T}}\bar{\mathbf{F}},\\
\frac{\partial \varphi^g[n]}{\partial \theta_{\mathrm{BM}}} &= j\frac{2\pi}{\lambda_c} d\cos\theta_{\mathrm{BM}}\rho_{\mathrm{BM}} e^{j\left(\phi_{\mathrm{BM}}-2\pi n\frac{\tau_{\mathrm{BM}}}{NT}\right)}\alpha(\theta_{\mathrm{BM}})^{\mathrm{T}}\mathbf{B}\bar{\mathbf{F}},\\
\frac{\partial \varphi^g[n]}{\partial \rho_{\mathrm{BM}}} &= e^{j\phi_{\mathrm{BM}}} e^{-j2\pi n\frac{\tau_{\mathrm{BM}}}{NT}} \alpha(\theta_{\mathrm{BM}})^{\mathrm{T}}\bar{\mathbf{F}},\\
\frac{\partial \varphi^g[n]}{\partial \phi_{\mathrm{BM}}} &= j\rho_{\mathrm{BM}} e^{j\phi_{\mathrm{BM}}} e^{-j2\pi n\frac{\tau_{\mathrm{BM}}}{NT}} \alpha(\theta_{\mathrm{BM}})^{\mathrm{T}}\bar{\mathbf{F}},\\
\frac{\partial \varphi^g[n]}{\partial \tau_{\mathrm{RM}}} &= \frac{-j2\pi n}{NT}\rho_{\mathrm{RM}} e^{j\phi_{\mathrm{RM}}} e^{-j2\pi n\frac{\tau_{\mathrm{RM}}}{NT}} \alpha(\theta_{\mathrm{RM}})^{\mathrm{T}}\Omega^g\left(\mathbf{H}_{\mathrm{BR}}[n]\right)^{\mathrm{T}}\bar{\mathbf{F}},\\
\frac{\partial \varphi^g[n]}{\partial \theta_{\mathrm{RM}}} &= j\frac{2\pi}{\lambda_c} d\cos\theta_{\mathrm{RM}}\rho_{\mathrm{RM}} e^{j\phi_{\mathrm{RM}}} e^{-j2\pi n\frac{\tau_{\mathrm{RM}}}{NT}} \alpha(\theta_{\mathrm{RM}})^{\mathrm{T}}\bar{\mathbf{B}}\\
&\quad\times \Omega^g\left(\mathbf{H}_{\mathrm{BR}}[n]\right)^{\mathrm{T}}\bar{\mathbf{F}},\\
\frac{\partial \varphi^g[n]}{\partial \rho_{\mathrm{R}}} &= \frac{1}{\rho_{\mathrm{BR}}} e^{j\phi_{\mathrm{RM}}} e^{-j2\pi n\frac{\tau_{\mathrm{RM}}}{NT}} \alpha(\theta_{\mathrm{RM}})^{\mathrm{T}}\Omega^g\left(\mathbf{H}_{\mathrm{BR}}[n]\right)^{\mathrm{T}}\bar{\mathbf{F}},\\
\frac{\partial \varphi^g[n]}{\partial \phi_{\mathrm{R}}} &= j\rho_{\mathrm{RM}} e^{j\phi_{\mathrm{RM}}} e^{-j2\pi n\frac{\tau_{\mathrm{RM}}}{NT}} \alpha(\theta_{\mathrm{RM}})^{\mathrm{T}}\Omega^g\left(\mathbf{H}_{\mathrm{BR}}[n]\right)^{\mathrm{T}}\bar{\mathbf{F}},
\end{aligned} \tag{28}$$

where $\bar{\mathbf{F}} = P\sqrt{\kappa_t\kappa_r}\mathbf{F}^g[n]\mathbf{z}^g[n]$, $\mathbf{B} = \mathrm{diag}[0, 1, \ldots, M_{\mathrm{B}} - 1]$ for $\mathbf{B} \in \mathbb{R}^{M_{\mathrm{B}}\times M_{\mathrm{B}}}$ and $\bar{\mathbf{B}} = \mathrm{diag}[0, 1, \ldots, M_{\mathrm{R}} - 1]$ for $\bar{\mathbf{B}} \in \mathbb{R}^{M_{\mathrm{R}}\times M_{\mathrm{R}}}$.

Additionally, the derivatives of the noise variance C_y with respect to the unknown channel parameters vector can be calculated as follows

$$\begin{aligned}
\frac{\partial C_y}{\partial \rho_{\mathrm{BM}}} &= 2P(1-\kappa_t\kappa_r)M_{\mathrm{B}}\rho_{\mathrm{BM}},\\
\frac{\partial C_y}{\partial \rho_{\mathrm{R}}} &= 2P(1-\kappa_t\kappa_r)M_{\mathrm{B}}M_{\mathrm{R}}^2\rho_{\mathrm{BR}}\rho_{\mathrm{RM}}.\\
\frac{\partial C_y}{\partial \tau_{\mathrm{BM}}} &= \frac{\partial C_y}{\partial \theta_{\mathrm{BM}}} = \frac{\partial C_y}{\partial \phi_{\mathrm{BM}}} = \frac{\partial C_y}{\partial \tau_{\mathrm{RM}}} = \frac{\partial C_y}{\partial \theta_{\mathrm{RM}}} = \frac{\partial C_y}{\partial \phi_{\mathrm{R}}} = 0.
\end{aligned} \tag{29}$$

Now, the FIM of the position parameters vector $\mathbf{J}_\mu \in \mathbb{R}^{7\times 7}$ is obtained by utilizing the transformation the following formula

$$\mathbf{J}_\mu = \mathbf{T}\mathbf{J}_\beta\mathbf{T}^{\mathrm{T}}, \tag{30}$$

where the transformation matrix is given as

$$\mathbf{T} \in \mathbb{R}^{7\times 8} \overset{(\mathrm{def})}{=} \frac{\partial \boldsymbol{\beta}^{\mathrm{T}}}{\partial \boldsymbol{\mu}} =$$

$$\begin{bmatrix}
\frac{\partial \tau_{\mathrm{BM}}}{\partial p_x} & \frac{\partial \theta_{\mathrm{BM}}}{\partial p_x} & \frac{\partial \rho_{\mathrm{BM}}}{\partial p_x} & \frac{\partial \phi_{\mathrm{BM}}}{\partial p_x} & \frac{\partial \tau_{\mathrm{RM}}}{\partial p_x} & \frac{\partial \theta_{\mathrm{RM}}}{\partial p_x} & \frac{\partial \rho_{\mathrm{R}}}{\partial p_x} & \frac{\partial \phi_{\mathrm{R}}}{\partial p_x}\\
\frac{\partial \tau_{\mathrm{BM}}}{\partial p_y} & \frac{\partial \theta_{\mathrm{BM}}}{\partial p_y} & \frac{\partial \rho_{\mathrm{BM}}}{\partial p_y} & \frac{\partial \phi_{\mathrm{BM}}}{\partial p_y} & \frac{\partial \tau_{\mathrm{RM}}}{\partial p_y} & \frac{\partial \theta_{\mathrm{RM}}}{\partial p_y} & \frac{\partial \rho_{\mathrm{R}}}{\partial p_y} & \frac{\partial \phi_{\mathrm{R}}}{\partial p_y}\\
\frac{\partial \tau_{\mathrm{BM}}}{\partial \rho_{\mathrm{BM}}} & \frac{\partial \theta_{\mathrm{BM}}}{\partial \rho_{\mathrm{BM}}} & \frac{\partial \rho_{\mathrm{BM}}}{\partial \rho_{\mathrm{BM}}} & \frac{\partial \phi_{\mathrm{BM}}}{\partial \rho_{\mathrm{BM}}} & \frac{\partial \tau_{\mathrm{RM}}}{\partial \rho_{\mathrm{BM}}} & \frac{\partial \theta_{\mathrm{RM}}}{\partial \rho_{\mathrm{BM}}} & \frac{\partial \rho_{\mathrm{R}}}{\partial \rho_{\mathrm{BM}}} & \frac{\partial \phi_{\mathrm{R}}}{\partial \rho_{\mathrm{BM}}}\\
\frac{\partial \tau_{\mathrm{BM}}}{\partial \phi_{\mathrm{BM}}} & \frac{\partial \theta_{\mathrm{BM}}}{\partial \phi_{\mathrm{BM}}} & \frac{\partial \rho_{\mathrm{BM}}}{\partial \phi_{\mathrm{BM}}} & \frac{\partial \phi_{\mathrm{BM}}}{\partial \phi_{\mathrm{BM}}} & \frac{\partial \tau_{\mathrm{RM}}}{\partial \phi_{\mathrm{BM}}} & \frac{\partial \theta_{\mathrm{RM}}}{\partial \phi_{\mathrm{BM}}} & \frac{\partial \rho_{\mathrm{R}}}{\partial \phi_{\mathrm{BM}}} & \frac{\partial \phi_{\mathrm{R}}}{\partial \phi_{\mathrm{BM}}}\\
\frac{\partial \tau_{\mathrm{RM}}}{\partial \rho_{\mathrm{R}}} & \frac{\partial \theta_{\mathrm{RM}}}{\partial \rho_{\mathrm{R}}} & \frac{\partial \rho_{\mathrm{RM}}}{\partial \rho_{\mathrm{R}}} & \frac{\partial \phi_{\mathrm{RM}}}{\partial \rho_{\mathrm{R}}} & \frac{\partial \tau_{\mathrm{RM}}}{\partial \rho_{\mathrm{R}}} & \frac{\partial \theta_{\mathrm{RM}}}{\partial \rho_{\mathrm{R}}} & \frac{\partial \rho_{\mathrm{R}}}{\partial \rho_{\mathrm{R}}} & \frac{\partial \phi_{\mathrm{R}}}{\partial \rho_{\mathrm{R}}}\\
\frac{\partial \tau_{\mathrm{RM}}}{\partial \phi_{\mathrm{R}}} & \frac{\partial \theta_{\mathrm{RM}}}{\partial \phi_{\mathrm{R}}} & \frac{\partial \rho_{\mathrm{RM}}}{\partial \phi_{\mathrm{R}}} & \frac{\partial \phi_{\mathrm{RM}}}{\partial \phi_{\mathrm{R}}} & \frac{\partial \tau_{\mathrm{RM}}}{\partial \phi_{\mathrm{R}}} & \frac{\partial \theta_{\mathrm{RM}}}{\partial \phi_{\mathrm{R}}} & \frac{\partial \rho_{\mathrm{R}}}{\partial \phi_{\mathrm{R}}} & \frac{\partial \phi_{\mathrm{R}}}{\partial \phi_{\mathrm{R}}}\\
\frac{\partial \tau_{\mathrm{RM}}}{\partial \Delta} & \frac{\partial \theta_{\mathrm{RM}}}{\partial \Delta} & \frac{\partial \rho_{\mathrm{RM}}}{\partial \Delta} & \frac{\partial \phi_{\mathrm{RM}}}{\partial \Delta} & \frac{\partial \tau_{\mathrm{RM}}}{\partial \Delta} & \frac{\partial \theta_{\mathrm{RM}}}{\partial \Delta} & \frac{\partial \rho_{\mathrm{R}}}{\partial \Delta} & \frac{\partial \phi_{\mathrm{R}}}{\partial \Delta}
\end{bmatrix}.$$

The elements of the transformation matrix depends on the geometric relationships between the estimated parameters in $\boldsymbol{\beta}$ vector and position and clock offset parameters in $\boldsymbol{\mu}$ vector, where these geometric relationship are provided in (26). Accordingly, the elements of the transformation matrix $\mathbf{T}$ are zero except

$$\begin{aligned}
\frac{\partial \rho_{\mathrm{BM}}}{\partial \rho_{\mathrm{BM}}} &= \frac{\partial \phi_{\mathrm{BM}}}{\partial \phi_{\mathrm{BM}}} = \frac{\partial \rho_{\mathrm{R}}}{\partial \rho_{\mathrm{R}}} = \frac{\partial \phi_{\mathrm{R}}}{\partial \phi_{\mathrm{R}}} = \frac{\partial \tau_{\mathrm{BM}}}{\partial \Delta} = \frac{\partial \tau_{\mathrm{RM}}}{\partial \Delta} = 1,\\
\frac{\partial \tau_{\mathrm{BM}}}{\partial p_x} &= \frac{p_x}{c\sqrt{p_x^2+p_y^2}},\\
\frac{\partial \tau_{\mathrm{BM}}}{\partial p_y} &= \frac{p_y}{c\sqrt{p_x^2+p_y^2}},\\
\frac{\partial \theta_{\mathrm{BM}}}{\partial p_x} &= \frac{-p_y/p_x^2}{1+\left(p_y/p_x\right)^2},\\
\frac{\partial \theta_{\mathrm{BM}}}{\partial p_y} &= \frac{1/p_x}{1+\left(p_y/p_x\right)^2},\\
\frac{\partial \tau_{\mathrm{RM}}}{\partial p_x} &= \frac{\left(p_x-r_x\right)}{c\sqrt{\left(p_x-r_x\right)^2+\left(p_y-r_y\right)^2}},\\
\frac{\partial \tau_{\mathrm{RM}}}{\partial p_y} &= \frac{\left(p_y-r_y\right)}{c\sqrt{\left(p_x-r_x\right)^2+\left(p_y-r_y\right)^2}},\\
\frac{\partial \theta_{\mathrm{RM}}}{\partial p_x} &= \frac{-\frac{p_y-r_y}{\left(p_x-r_x\right)^2}}{1+\left(\frac{p_y-r_y}{p_x-r_x}\right)^2},\\
\frac{\partial \theta_{\mathrm{RM}}}{\partial p_y} &= \frac{1/\left(p_x-r_x\right)}{1+\left(\frac{p_y-r_y}{p_x-r_x}\right)^2}.
\end{aligned} \tag{31}$$

Finally, the PEB and the SEB of the RIS-assisted *mm*-wave MISO-OFDM system are calculated from

$$\mathrm{PEB} = \sqrt{\left[\left(\mathbf{J}_\mu\right)^{-1}\right]_{(1,1)} + \left[\left(\mathbf{J}_\mu\right)^{-1}\right]_{(2,2)}}, \tag{32}$$

$$\mathrm{SEB} = \sqrt{\left[\left(\mathbf{J}_\mu\right)^{-1}\right]_{(7,7)}}. \tag{33}$$

IV. SIMULATION RESULTS

This section discusses the harmful effects of the HWI on the accuracy of the joint localization and synchronization process in a RIS-assisted *mm*-wave MISO-OFDM system. The system operates at $f_c = 60$ GHz with a bandwidth of $B = 40$ MHz, and $N = 20$ sub-carriers, where the bandwidth achieves the narrow band condition

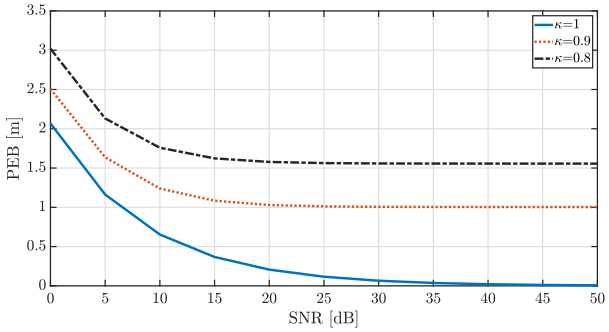

FIGURE 3. PEB v.s the transmission power with different κ in the RIS-assisted system.

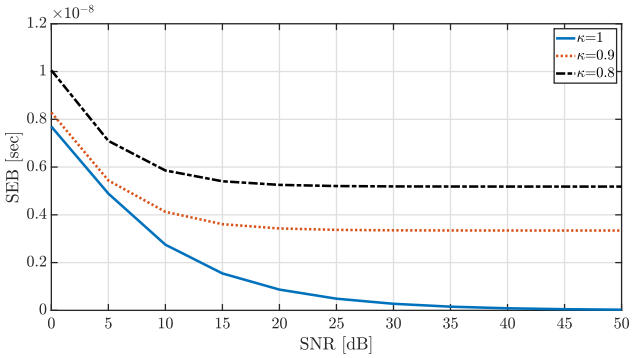

FIGURE 4. SEB v.s the transmission power with different κ in the RIS-assisted system.

as $\lambda_1 = \lambda_2 = \cdots \lambda_{20} \approx 5$ mm. The unknown position MS observes $G = 20$ transmissions of a known signal over $K = 1$ simultaneously transmitted beams from a known position BS. Based on these observations over the OFDM sub-carriers, the MS that is equipped with a single antenna performs the joint self-localization and self-synchronization processes by measuring the TOAs (τ_{BM} and τ_{RM}) and AODs (θ_{BM} and θ_{RM}). In the proposed system, the BS is equipped with $M = 10$ antennas, while the RIS is equipped with $M_{\mathrm{R}} = 40$ elements and has a phase control matrix ($\boldsymbol{\Omega}^g$) of which is generated by assuming equiprobable binary random variables.

It is worth noting that the transceivers of the BS and MS are non-ideal in both scenarios since they suffer from HWIs with distortion coefficients $\kappa_t = \kappa_r$ for simplicity. The HWIs with distortion coefficients κ can be practically measured from the error vector magnitude (EVM) information that is specified on the data sheets of the RF transceivers, and given by $\kappa = 1 - \mathrm{EVM}^2$ [22]. Finally, the error bounds of the localization and synchronization estimation processes are presented in terms of CRLB, since it provides the lower performance limits of the localization and synchronization processes.

With the aim of investigating the impact of increasing transmission power on the accuracy of the localization process, Figs. 2 and 3 plot the PEB against SNR for different HWI distortion levels. In particular, Fig. 2 presents the localization process in the conventional *mm*Wave MISO-OFDM from [33] (without an RIS), which assumes ideal synchronization, while Fig. 3 presents the accuracy in a more

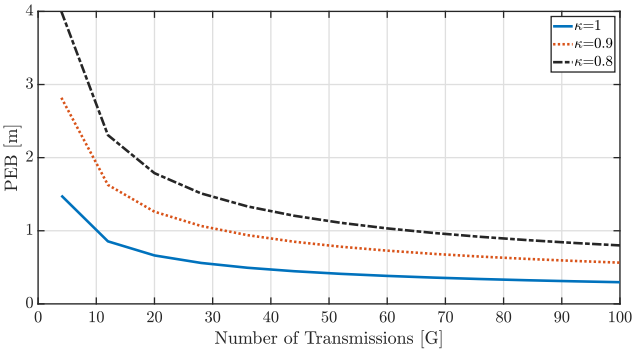

FIGURE 5. PEB v.s the number of transmissions for different values of κ.

practical system: the case of performing the localization and synchronization jointly. As the quality of the received signal increases by strengthening the transmission power, the accuracy of localization process accuracy. Unfortunately, since the HWI distortion limits the SNR as in (23), the accuracy of the localization process are bounded to a non-zero value, while the PEB values asymptotically approach zero in ideal hardware conditions, i.e., $\kappa_t = \kappa_r = 1$. The same figures also confirm that as the HWI distortion increases, the accuracy of localization decreases. Besides, the comparison between the two figures reveals that the accuracy of the localization process in the case of perfect synchronization is higher than that of the joint localization-synchronization in the asynchronous system.

Fig. 4 depicts the reason behind the differences in the accuracy of the localization processes of the synchronous and asynchronous cases by presenting the error in the synchronization process against the SNR. Moreover, Fig. 4 presents the effect HWIs at both the transmitter and receiver sides on the synchronization process of the RIS-assisted *mm*-wave MISO-OFDM. It is clear that increasing the transmission power tends the synchronization error to zero in the ideal hardware case, while the existence of HWIs saturates the SEB to a non-zero level. This occurs because increasing the transmission power in the presence of the HWIs boosts both the non-noisy signal $\varphi^g[n]$ and the HWI distortion term C_y simultaneously as seen from (20) and (21).

Besides, Fig.4 confirms that the destructive effects of the HWI on the synchronization accuracy gets worse with decreasing values of κ. In the low power value range, the HWI distortion is small and thus, the accuracy of the processes is similar regardless of the κ values, while the differences in accuracy become larger in the range of high power.

Figs. 5 and 6 investigate enhancing the joint localization and synchronization process through increasing the number of transmission G. They show that increasing G enhances the accuracy of the localization and synchronization processes. In both figures, the accuracy is affected by the amount of distortion stemming from the HWI. Although the increasing number of transmission enhances the overall system performance, it means reducing the data-rate in the meantime. Hence, a favorable trade-off should be managed between these two based on the parameter G.

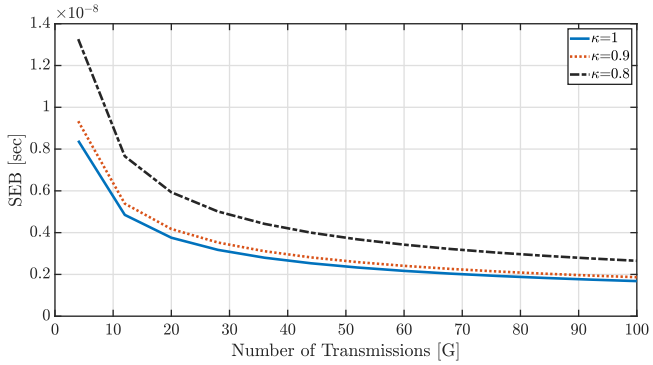

FIGURE 6. SEB v.s the number of transmissions for different values of κ.

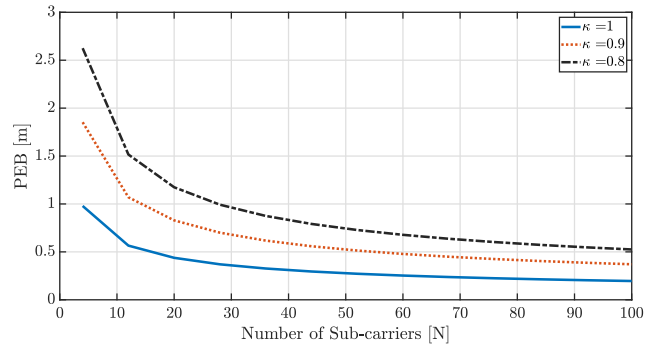

FIGURE 7. PEB v.s the number of sub-carriers for different values of κ.

The effect of increasing the bandwidth on the accuracy of the joint localization and synchronization processes of the RIS-assisted *mm*-wave MISO OFDM system is depicted in Figs. 7 and 8, respectively. It is clear that increasing N, and thus the bandwidth, enhances the accuracy for both the ideal and the non-ideal equipment. Moreover, the deterioration in the accuracy of localization and synchronization depends on the level of HWI distortion.

The effect of increasing the number of transmitter antennas on the PEB and SEB performance in the presence of the HWI is investigated in Figs. 9 and 10, respectively. However, it is observed that accelerating the number of the transmitter antennas after $M_B = 10$ provides almost no improvement in the accuracy of the localization and synchronization for non-ideal hardware cases. This is because, in the non-ideal hardware, the HWI distortion levels increase with increasing the number of antennas. On the other hand, increasing the number of antennas continuously enhances the accuracy of the localization and synchronization processes with the ideal hardware cases.

Lastly, in Figs. 11 and 12, the accuracy of the localization and synchronization processes is presented with respect to increasing the number of reflecting elements on the RIS. As seen from these figures, increasing M_{R} obviously enhances the localization and synchronization accuracy for all values of κ. Most importantly, since the reflecting elements are passive and then don't produce distortion, they enhance the localization and synchronization accuracy despite to the HWI, where it is observed in the figures that the PEB and

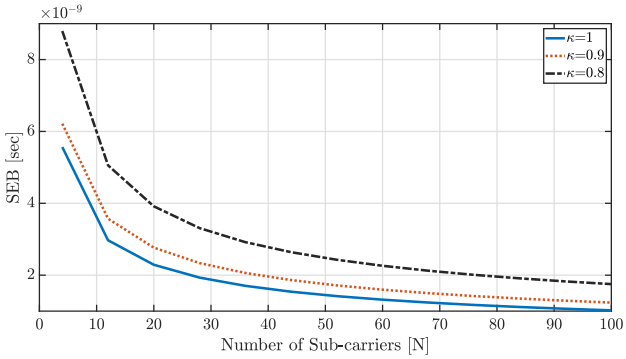

FIGURE 8. SEB v.s the number of sub-carriers for different values of κ.

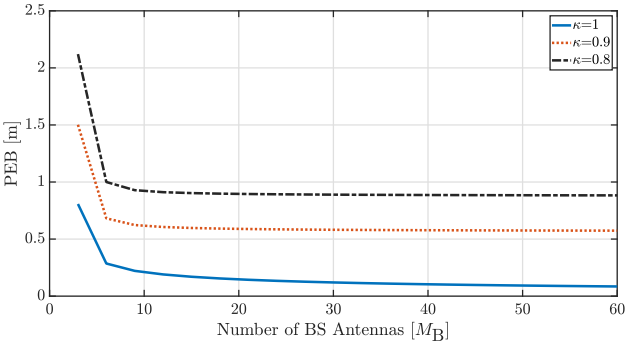

FIGURE 9. PEB v.s the number of BS antennas for different values of κ.

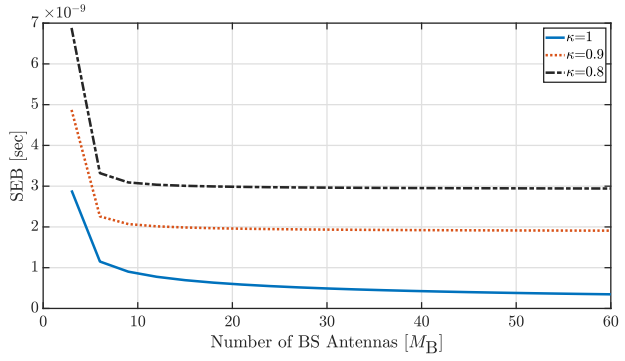

FIGURE 10. SEB v.s the number of BS antennas for different values of κ.

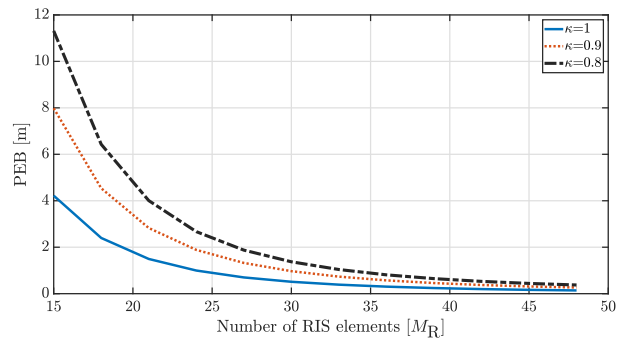

FIGURE 11. PEB v.s the number of RIS elements for different values of κ.

SEB values with non-ideal hardware approximate to the ideal hardware for relatively high number of reflectors. In other words, the destructive effects of the HWIs on the joint

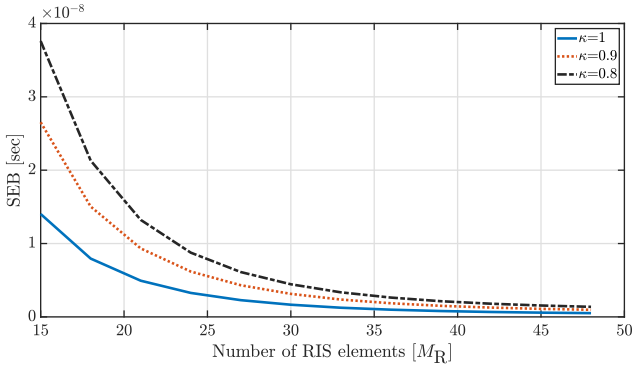

FIGURE 12. SEB v.s the number of RIS elements for different values of κ.

localization and synchronization processes can be mitigated by using an RIS with reasonably high number of reflecting elements on it in a *mm*-wave MISO OFDM system.

V. CONCLUSION

This paper studies the impacts of HWIs on the joint localization and synchronization process of the RIS-assisted *mm*-Wave MISO-OFDM systems. Considering imperfect transceivers at the BS and MS, a well-known pilot is broadcasted from the transmitter to the receiver that performs the self joint localization and synchronization processes. The FIM of the channel parameters is calculated and then the transformation matrix is computed to obtain the FIM of the localization vector, whose inverse provides the CRLB. Finally, computer simulation results illustrate a degradation in localization and synchronization accuracy due to the non-ideal transceivers at the BS and MS. Moreover, the simulation results indicate to that enhancing the accuracy of the localization and synchronization through varying effective SNR values, increasing the number of pilot transmissions, the bandwidth or the number of BS antennas is limited by the HWI distortion. Fortunately, the computer simulations show that increasing the number of the reflecting elements of RIS elements has a significant role in mitigating destructive effects of the HWIs on the PEB and SEB performance and achieving the ideal hardware's accuracy. Considering machine learning approaches, which have fashionable applications to communication studies nowadays, for joint localization-synchronization would be an interesting direction for future research.

REFERENCES

[1] C.-X. Wang *et al.*, "Cellular architecture and key technologies for 5G wireless communication networks," *IEEE Commun. Mag.*, vol. 52, no. 2, pp. 122–130, Feb. 2014.

[2] A. Shahmansoori, G. E. Garcia, G. Destino, G. Seco-Granados, and H. Wymeersch, "Position and orientation estimation through mmWave MIMO in 5G systems," *IEEE Trans. Wireless Commun.*, vol. 17, no. 3, pp. 1822–1835, Mar. 2018.

[3] Z. Abu-Shaban, H. Wymeersch, T. Abhayapala, and G. Seco-Granados, "Single-anchor two-way localization bounds for 5G mmWave systems: Two protocols," *IEEE Trans. Veh. Technol.*, vol. 69, no. 6, pp. 6388–6400, Jun. 2020.

[4] K. Witrisal *et al.*, "High-accuracy localization for assisted living: 5G systems will turn multipath channels from foe to friend," *IEEE Signal Process. Mag.*, vol. 33, no. 2, pp. 59–70, Mar. 2016.

[5] B. Zhou, A. Liu, and V. Lau, "Successive localization and beamforming in 5G mmWave MIMO communication systems," *IEEE Trans. Signal Process.*, vol. 67, no. 6, pp. 1620–1635, Mar. 2019.

[6] Z. Abu-Shaban, X. Zhou, T. D. Abhayapala, G. Seco-Granados, and H. Wymeersch, "Error bounds for uplink and downlink 3D localization in 5G milimeter-wave systems," *IEEE Trans. Wireless Commun.*, vol. 17, no. 8, pp. 4939–4954, Aug. 2018.

[7] Z. Marzi, D. Ramasamy, and U. Madhow, "Compressive channel estimation and tracking for large arrays in mm-Wave picocells," *IEEE J. Sel. Top. Signal Process.*, vol. 10, no. 3, pp. 514–527, Apr. 2016.

[8] A. Guerra, F. Guidi, and D. Dardari, "Position and orientation error bound for wideband massive antenna arrays," in *Proc. Int. Conf. Commun. Workshop (ICC)*, London, U.K., Jun. 2015, pp. 853–858.

[9] A. E. Canbilen, "Performance analysis of RIS-assisted SM with I/Q imbalance," *Phys. Commun.*, vol. 49, Dec. 2021, Art. no. 101473.

[10] Q. Wu and R. Zhang, "Intelligent reflecting surface enhanced wireless network via joint active and passive beamforming," *IEEE Trans. Wireless Commun.*, vol. 18, no. 11, pp. 5394–5409, Nov. 2019.

[11] D. Tubail, B. Cenikliogl u, A. E. Canbilen, I. Develi, and S. Ikki, "Error bounds for 3D localization and maximum likelihood estimation of mm-Wave MISO OFDM systems in the presence of hardware impairments," *IEEE Commun. Lett.*, early access, Jun. 27, 2022, doi: 10.1109/LCOMM.2022.3186789.

[12] A. Elzanaty, A. Guerra, F. Guidi, and M. Alouini, "Reconfigurable intelligent surfaces for localization: Position and orientation error bounds," Aug. 2020, *arXiv:2009.02818*.

[13] J. He, H. Wymeersch, L. Kong, O. Silven, and M. Juntti, "Large intelligent surface for positioning in millimeter wave MIMO systems," in *Proc. IEEE Veh. Technol. Conf.*, Antwerp, Belgium, May 2020, pp. 1–5.

[14] A. Fascista, A. Coluccia, H. Wymeersch, and G. Seco-Granados, "RIS-aided joint localization and synchronization with a single-antenna MmWave receiver," 2020, *arXiv:2010.14825*.

[15] H. Wymeersch, J. He, B. Denis, A. Clemente, and M. Juntti, "Radio localization and mapping with reconfigurable intelligent surfaces: Challenges, opportunities, and research directions," *IEEE Veh. Technol. Mag.*, vol. 15, no. 4, pp. 52–61, Dec. 2020.

[16] F. Ghaseminajm, Z. Abu-Shaban, S. Ikki, H. Wymeersch, and C. R. Benson, "Localization error bounds for 5G mmWave systems under I/Q imbalance," *IEEE Trans. Veh. Technol.*, vol. 69, no. 7, pp. 7971–7975, Jul. 2020.

[17] T. Zhou, K. Xu, Z. Shen, W. Xie, D. Zhang, and J. Xu, "AoA-based positioning for aerial intelligent reflecting surface-aided wireless communications: An angle-domain approach," *IEEE Wireless Commun. Lett.*, vol. 11, no. 4, pp. 761–765, Apr. 2022.

[18] H. Zhang, H. Zhang, B. Di, K. Bian, Z. Han, and L. Song, "MetaLocalization: Reconfigurable intelligent surface aided multi-user wireless indoor Localization," *IEEE Trans. Wireless Commun.*, vol. 20, no. 12, pp. 7743–7757, Dec. 2021.

[19] A. E. Canbilen, E. Basar, and S. Ikki, "Reconfigurable intelligent surface-assisted space shift keying," *IEEE Wireless Commun. Lett.*, vol. 9, no. 9, pp. 1495–1499, Sep. 2020.

[20] A. Fascista, M. Keskin, A. Coluccia, H. Wymeersch, and G. Seco-Granados, "RIS-aided joint Localization and synchronization with a single-antenna receiver: Beamforming design and low-complexity estimation," *IEEE J. Sel. Top. Signal Process*, vol. 16, no. 5, pp. 1141–1156, Aug. 2022.

[21] D. Tubail, B. Cenikliogl u, A. E. Canbilen, I. Develi, and S. Ikki, "The effect of hardware impairments on the error bounds of localization and maximum likelihood estimation of mmWave MISO-OFDM systems," *IEEE Trans. Veh. Technol.*, submitted for publication.

[22] E. Björnson, J. Hoydis, and L. Sanguinetti, *Massive MIMO Networks: Spectral, Energy, and Hardware Efficiency*, vol. 11. Hanover, MA, USA: Now Publ., Inc., Nov. 2017. [Online]. Available: http://www.nowpublishers.com

[23] B. Cenikliogl u, I. Develi, A. E. Canbilen, and M. Lafci, "Analysis of average bit error rate for OFDM-IM systems with hardware impairments over Nakagami-m and Weibull fading channels," in *Proc. Int. Conf. Comput. Commun. Security Intell. Syst.*, 2022, pp. 1–6.

[24] H. Mehrpouyan, M. Matthaiou, R. Wang, G. Karagiannidis, and Y. Hua, "Hybrid millimeter-wave systems: A novel paradigm for HetNets," *IEEE Commun. Mag.*, vol. 53, no. 1, pp. 216–221, Jan. 2015.

[25] F. Ghaseminajm, E. Saleh, M. M. Alsmadi, and S. Ikki, "Localization error bounds for 5G mmWave systems under hardware impairments," in *Proc. IEEE 32nd Annu. Int. Symp. Pers. Indoor Mobile Radio Commun.*, Helsinki, Finland, Sep. 2021, pp. 1228–1233.
[26] F. Ghaseminajm, M. Alsamdi, and S. S. Ikki, "Error bounds for localization in *mm*Wave MIMO systems: Effects of hardware impairments considering perfect and imperfect clock synchronization," *IEEE Syst J.*, early access, Apr. 12, 2022, doi: 10.1109/JSYST.2022.3163021.
[27] R. M. Vaghefi and R. M. Buehrer, "Joint TOA-based sensor synchronization and localization using semidefinite programming," in *Proc. IEEE Int. Conf. Commun. (ICC)*, Sydney, NSW, Australia, Jun. 2014, pp. 520–525.
[28] J. Liu, Z. Wang, J. Cui, S. Zhou, and B. Yang, "A joint time synchronization and localization design for mobile underwater sensor networks," *IEEE Trans. Mobile Comput.*, vol. 15, no. 3, pp. 530–573, Mar. 2016.
[29] J. Zheng and Y.-C. Wu, "Robust joint localization and time synchronization in wireless sensor networks with bounded anchor uncertainties," in *Proc. IEEE Int. Conf. Acoust. Speech Signal Process.*, Taipei, Taiwan, Apr. 2009, pp. 2793–2796.
[30] A. Fascista, M. F. Keskin, A. Coluccia, H. Wymeersch, and G. Seco-Granados, "RIS-aided joint localization and synchronization with a single-antenna receiver: Beamforming design and low-complexity estimation," *IEEE J. Sel. Top. Signal Process.*, vol. 16, no. 5, pp. 1141–1156, Aug. 2022.
[31] A. Elzanaty, A. Guerra, F. Guidi, and M.-S. Alouini, "Reconfigurable intelligent surfaces for localization: Position and orientation error bounds," *IEEE Trans. Signal Process.*, vol. 69, no. 1, pp. 5386–5402, Aug. 2021.
[32] A. Fascista, A. Coluccia, H. Wymeersch, and G. Seco-Granados, "RIS-aided joint localization and synchronization with a single-antenna mmwave receiver," in *Proc. IEEE Int. Conf. Acoust., Speech Signal Process. (ICASSP)*, 2021, pp. 4455–4459.
[33] A. Fascista, A. Coluccia, H. Wymeersch, and G. Seco-Granados, "Millimeter-wave downlink positioning with a single-antenna receiver," *IEEE Trans. Wireless Commun.*, vol. 18, no. 9, pp. 4479–4490, Sep. 2019.
[34] A. Fascista, A. Coluccia, H. Wymeersch, and G. Seco-Granados, "Downlink single-snapshot localization and mapping with a single-antenna receiver," *IEEE Trans. Wireless Commun.*, vol. 20, no. 7, pp. 4672–4684, Jul. 2021.
[35] A. Fascista, A. D. Monte, A. Coluccia, H. Wymeersch, and G. Seco-Granados, "Low-complexity downlink channel estimation in mmWave multiple-input single-output systems," *IEEE Wireless Commun. Lett.*, vol. 11, no. 3, pp. 518–522, Mar. 2022.
[36] B. Zhou, R. Wichman, L. Zhang, and Z. Luo, "Simultaneous Localization and channel estimation for 5G mmWave MIMO communications," in *Proc. IEEE 32nd Annu. Int. Symp. Pers. Indoor Mobile Radio Commun. (PIMRC)*, Helsinki, Finland, Sep. 2021, pp. 853–858.
[37] A. Alkhateeb and R. W. Heath, "Frequency selective hybrid Precoding for limited feedback Millimeter wave systems," *IEEE Trans. Commun.*, vol. 64, no. 5, pp. 1801–1818, May 2016.
[38] S. M. Kay, *Fundamentals of Statistical Signal Processing: Estimation Theory*, vol. 1. Englewood Cliffs, NJ, USA: Prentice-hall, Mar. 1993.

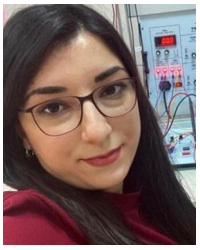

BUSRA CENIKLIOGLU (Graduate Student Member, IEEE) received the B.S. and M.S. degrees in electrical and electronics engineering from Erciyes University, Kayseri, Turkey, in 2016 and 2018, where she is currently pursuing the Ph.D. degree in electrical and electronics engineering. From 2021 to 2022, she was with the Department of Electrical Engineering, Lakehead University, Thunder Bay, ON, Canada, as a Visiting Researcher. She is currently a Research Assistant with the Department of Electrical and Electronics Engineering, Nuh Naci Yazgan University, Kayseri. Her research interests include this topics: MISO systems, index modulation, reconfigurable intelligent surfaces, hardware impairments, localization, and B5G.

DEEB ASSAD TUBAIL received the B.S. degree (Hons.) in electrical engineering and the M.Sc. degree (Hons.) in telecommunication from the Islamic University of Gaza, Palestine, in 2009 and 2014, respectively. He is currently pursuing the Ph.D. degree with the Electrical and Computer Engineering Department, Lakehead University, Canada, in 2020, where he is performing his research in wireless communication in estimation, localization and performance analysis. He performed his master's research in the Microwave area in coupled-resonators circuits and microwave devices field. After that, his research fields were wireless communication in physical-layer security, interference alignment, multiuser MIMO systems, and optimization.

AYSE ELIF CANBILEN (Member, IEEE) received the Ph.D. degree from Konya Technical University in 2019. From 2017 to 2018, she was with the Department of Electrical Engineering, Lakehead University, Thunder Bay, ON, Canada, as a Visitor Researcher. She is currently an Assistant Professor with the Department of Electrical and Electronics Engineering, Konya Technical University, Konya, Turkey. Her primary research interests include beyond 5G systems, spatial modulation techniques, reconfigurable intelligent surfaces, and visible light communications. She has been serving as a Reviewer for the IEEE TRANSACTIONS ON COMMUNICATIONS, IEEE TRANSACTIONS ON WIRELESS COMMUNICATIONS, IEEE TRANSACTIONS ON VEHICULAR TECHNOLOGY, IEEE COMMUNICATIONS LETTERS, and IEEE ACCESS.

IBRAHIM DEVELI (Senior Member, IEEE) received the B.S., M.S., and Ph.D. degrees from Erciyes University, Turkey, in 1995, 1997, and 2003, respectively. From 1995 to 2003, he was a Research Assistant with the Department of Electronics Engineering, Erciyes University, where he is currently a Professor. He teaches courses in wireless communications, and his current research interests are in cooperative communications, MIMO systems, spread spectrum communications, multiuser communications, wireless networks, and the applications of neural networks to multiuser communication systems. He has been a member of the TPC for a large number of major international conferences, such as IEEE ICC, IEEE GLOBECOM, IEEE BROADNETS, IEEE RWS, and IEEE WCNC. He currently serves as an Associate Editor for the *EURASIP Journal on Wireless Communications and Networking*. He is also on the Editorial Board of the *International Journal of Mobile Communications*.

SALAMA S. IKKI (Senior Member, IEEE) was a Visiting Research Professor with Nokia Scholarship, Aalto University, Helsinki, Finland, in 2022. He is currently an Associate Professor and the Research Chair of Wireless Communications with Lakehead University, Thunder Bay, ON, Canada. His research group has made substantial contributions to 4G and 5G wireless technologies. He is the author of more than 100 journals and conference papers and has more than 5500 citations and an H-index of 35. His group's current focuses on massive MIMO, cell-free massive MIMO, visible light communications, and wireless sensor networks. He received several awards for his research, teaching, and services.